Molecular dynamics simulation-based microstructure evolution and subsurface damage of Fe-Ni alloy grinding

Received 29 August 2022
Revised 26 September 2022
Accepted 26 September 2022

Weicheng Guo
University of Shanghai for Science and Technology, Shanghai, China
Chongjun Wu
College of Mechanical Engineering, Donghua University, Shanghai, China
Xiankai Meng
College of Mechanical Engineering, Jiangsu University, Zhenjiang, China, and
Chao Luo and Zhijian Lin
Aplos Machines Manufacturing (Shanghai) Co., Ltd., Shanghai, China

Abstract

Purpose – Molecular dynamics is an emerging simulation technique in the field of machining in recent years. Many researchers have tried to simulate different processing methods of various materials with the theory of molecular dynamics (MD), and some preliminary conclusions have been obtained. However, the application of MD simulation is more limited compared with traditional finite element model (FEM) simulation technique due to the complex modeling approach and long computation time. Therefore, more studies on the MD simulations are required to provide a reliable theoretical basis for the nanoscale interpretation of grinding process. This study investigates the crystal structures, dislocations, force, temperature and subsurface damage (SSD) in the grinding of iron-nickel alloy using MD analysis.

Design/methodology/approach – In this study the simulation model is established on the basis of the workpiece and single cubic boron nitride (CBN) grit with embedded atom method and Morse potentials describing the forces and energies between different atoms. The effects of grinding parameters on the material microstructure are studied based on the simulation results.

Findings – When CBN grit goes through one of the grains, the arrangement of atoms within the grain will be disordered, but other grains will not be easily deformed due to the protection of the grain boundaries. Higher grinding speed and larger cutting depth can cause greater impact of grit on the atoms, and more body-centered cubic (BCC) structures will be destroyed. The dislocations will appear in grain boundaries due to the rearrangement of atoms in grinding. The increase of grinding speed results in the more transformation from BCC to amorphous structures.

Originality/value – This study is aimed to study the grinding of Fe-Ni alloy (maraging steel) with single grit through MD simulation method, and to reveal the microstructure evolution within the affected range of SSD layer in the workpiece. The simulation model of polycrystalline structure of Fe-Ni maraging steel and grinding process of single CBN grit is constructed based on the Voronoi algorithm. The atomic accumulation,

This work was supported by the National Natural Science Foundation of China (Grant No. 52105470 and 52005098) and the Shanghai Natural Science Foundation (22ZR1402400). The authors wish to record their gratitude for the generous supports.

Declaration of Competing interest: The authors declare that they have no known competing financial interests or personal relationships that could have appeared to influence the work reported in this paper.

Journal of Intelligent Manufacturing and Special Equipment
Vol. 4 No. 1, 2023
pp. 47-63
Emerald Publishing Limited
e-ISSN: 2633-660X
p-ISSN: 2633-6596
DOI 10.1108/JIMSE-08-2022-0012

transformation of crystal structures, evolution of dislocations as well as the generation of SSD are discussed according to the simulation results.

Keywords Grinding, Crystal structures, Dislocations, Subsurface damage, Molecular dynamics
Paper type Research paper

1. Introduction

Iron nickel (Fe-Ni) alloy is a low frequency soft magnetic material with high permeability and low coercivity in weak magnetic fields, which is widely used as the crucial material to manufacture gyroscopes, accelerometers, firing pins in aeronautic and aerospace equipment. The service performance for these key components is extremely sensitive to the surface integrity, such as surface roughness, residual stress, microhardness, damage layer and so on (Zhou *et al.*, 2021a; Sun *et al.*, 2022; Guo *et al.*, 2021; Zhang *et al.*, 2022). Grinding is a kind of precision machining techniques and is often used as the last step to manufacture high-quality parts. Due to the micro size of inertial navigation components, the dimension of the grinding wheel is limited, and thus, the relative linear velocity between grinding wheel and workpiece is not able to reach a high level. Numerous studies have proved that higher wheel speed can significantly improve the surface integrity of the part because of less grinding force and smaller undeformed chip thickness. However, the quality of these high-performance parts in aeronautic and aerospace fields is difficult to be guaranteed during the micronanoscale grinding process, since the evolution of surface and subsurface microstructure of the part is different compared with those in the macrogrinding (Li *et al.*, 2022; Ding *et al.*, 2022; Lv *et al.*, 2020). Therefore, how to better understand the variation of material microstructure and accurately control the surface integrity in precision manufacturing conditions has become a major challenge for high-quality and high-efficient machining of key components in the aeronautic and aerospace equipment.

The traditional finite element model (FEM) tends to interpret the physical phenomena behind grinding in micro scale. Based on the material intrinsic model, the FEM simulation can be constructed to accurately quantify physical quantities such as stress, strain, strain rate, cutting force and cutting temperature during the grinding process, which in turn provides reference data for studying wheel wear, machining surface integrity and process optimization (Lerra *et al.*, 2022; Peng *et al.*, 2021; Chen *et al.*, 2022). The evolution of microstructure, such as plastic deformation, grain refinement, residual stress, etc., and physical and mechanical properties, namely hardness, yield strength, etc., can be graphically demonstrated by the simulation results, which can provide a distinct understanding of grinding process (Wan *et al.*, 2018; Guo *et al.*, 2020; Lan and Jiao, 2019).

In nanoscale grinding, material removal is generally the size of a dozen or even a few atoms, and in such a narrow cutting range, the effect on each atom is extremely complex. Meanwhile, the atomic motion in nanoscale grinding is different from the continuous motion in macroscopic grinding, which actually contains discrete phenomenon. Therefore, it is simply not feasible to adopt the macro-scale continuous medium theory to explain the nanoscale level with finite element analysis, and only the search for new methods and machining mechanisms under the nanoscale perspective can more accurately explain certain special phenomena that occur in the nanoscale grinding. Hence, molecular dynamics (MD) is proposed to study the behavior of atoms in the removal process (Li *et al.*, 2021; Ren *et al.*, 2018). The MD simulation explains the complex intrinsic interaction mechanism between abrasive grit and workpiece by revealing the basic process of atomic destruction in grinding. The conventional study on the relationship between grinding parameters and grinding energy is extended to the mechanisms of crystal structures, dislocations and crack initiations through MD (Huang *et al.*, 2021; Guo *et al.*, 2016; Li *et al.*, 2015).

In terms of the crystal structures, the nanogrinding process of copper-silicon with a single diamond abrasive grit is investigated by Xu *et al.* (2019) using MD simulations. The effects of

grinding depth, speed, and Cu thickness on material removal and defects are analyzed based on dislocations and phase transitions. The phase transitions from the face-centered cubic (FCC) to body-centered cubic (BCC) structures are accompanied by an increase in the atomic kinetic energy, while the kinetic energy is released as material recovers from elastic deformation. The transitions of the crystal structures will induce the phase transformation and residual stress. Zhao *et al.* (2022) adopt the MD method as the theoretical basis to study the mechanical response, phase transformation and residual stress of the single-crystal silicon during the nanogrinding process. The simulation results show that the grinding speed, temperature and grinding depth can affect the atomic movement process in the subsurface of the workpiece, thereby affecting the phase transformation and tensile residual stress of the workpiece. Zhou *et al.* (2021b) establish an MD model to simulate the belt grinding process of titanium alloy. The simulation results show that the titanium atoms on both sides and underneath the abrasive grit show different deformation patterns. In addition, the titanium atoms close to the cutting surface moved faster during cooling than those far from the cutting surface, which eventually resulted in the initiation of residual stress.

Dislocations have a great influence on the mechanical properties of materials, mainly in terms of toughness and strength. The material with more dislocations will have higher strength and less toughness, which means that the subsurface and surface of the workpiece is more prone to damage after grinding. By performing three-dimensional MD simulations, the effects of the tool radius, depth of cut and grinding speed on the grinding of Al–Si bilayers are studied by Wang *et al.* (2019) The brittle to ductile transition of bilayers, which strongly depends on the interface debond energy, has a key role in controlling the dislocation slipping mechanism. Li *et al.* (2014) study the mechanisms of subsurface damage (SSD) and material removal of monocrystalline copper under a nanoscale high speed grinding in MD simulations. The key factors that would influence the deformation of the material were the chip, dislocation movement, and workpiece deformation. The transition of deformation mechanisms depends on the competition between the dislocations and deformation twinning. Liu *et al.* (2022) investigate the nanogrinding process of single-crystal silicon carbide with MD. By changing the grinding depth, the atomic Y direction displacement, crystal defect, force, von Mises stress and the wear of abrasive are analyzed. With the increase in grinding depth, the atomic Y direction displacement, crystal defect, force and the wear of abrasive are gradually increasing.

MD is an emerging simulation technique in the field of machining in recent years. Many researchers have tried to simulate different processing methods of various materials with the theory of MD, and some preliminary conclusions have been obtained. However, the application of MD simulation is more limited compared with traditional FEM simulation technique due to the complex modeling approach and long computation time. Therefore, more studies on the MD simulations are required to provide a reliable theoretical basis for the nanoscale interpretation of grinding process. This study is aimed to study the grinding of Fe-Ni alloy (maraging steel) with single grit through MD simulation method and to reveal the microstructure evolution within the affected range of SSD layer in the workpiece. The simulation model of polycrystalline structure of Fe-Ni maraging steel and grinding process of single CBN grit is constructed based on the Voronoi algorithm. The atomic accumulation, transformation of crystal structures, evolution of dislocations as well as the generation of SSD are discussed according to the simulation results. The grinding experiment is carried out to qualitatively analyze the SSD of the workpiece by comparison of simulation and detection results.

2. Simulation methodology

2.1 Workpiece model in molecular dynamics

The accuracy of material properties determines the quality of the workpiece model. The properties of materials in MD simulations are determined by atomic mass, atomic coordinates

and interatomic potentials. Atomic mass can be obtained from the periodic table. The elements of workpiece material used in this study, namely maraging steel, are mostly composed of Fe and Ni (Yeqiong and Mufu, 2011), so that the model in the simulation will consist of these two elements. The atomic mass of Fe is 55.84 and the atomic mass of Ni is 58.69. The atomic coordinates depend on the crystal structure and atomic lattice constant. The maraging steel contains more than 86% BCC martensite and 13% BCC ferrite (Li *et al.*, 2016). Therefore, the material of workpiece model is set to the BCC primitive cell of 68% Fe and 32% Ni, and the lattice length is 0.2855 nm (Bonny *et al.*, 2009). For the cutting tool, namely CBN grit, its crystal structure is diamond structure and lattice constant is 0.3615 nm.

The atomic potential function is a physical curve that determines the atomic force and energy. Choosing the correct and accurate potential function is beneficial to get more correct results. In this study, the workpiece model mainly contains three kinds of interatomic forces, including the interaction of the metal atoms in the workpiece (Fe-Ni); the interaction between the workpiece and the grit (Fe-N, Ni-N, Fe-B, Ni-B); and the interaction of the atoms in the grit (B-N). Due to there are a lot of dislocations and gaps exit in the grain boundaries, the embedded atom method (EAM) (Foiles *et al.*, 1986; Daw *et al.*, 1993) potential function can describe the interatomic forces of Fe-Ni well. For Fe-N, Ni-N, Fe-B and Ni-B, Morse (Pei *et al.*, 2007; Zhang *et al.*, 2009) potential function can be easy to program and simple in form. Since the hardness of the CBN grit is much higher than the workpiece, it is not necessary to choose the potential function for B-N. Thus, the grit will be set as a rigid body.

The EAM potential function can accurately express the force and energy between Fe-Ni atoms, as shown in Equation (1).

$$E_{tot} = \frac{1}{2}\sum_{ij} \varnothing_{ij}(r_{ij}) + \sum_{i} F(\rho_i) \tag{1}$$

where $\varnothing_{ij}(r_{ij})$ is the repulsive interaction between atoms; $F(\rho_i)$ is the Mosaic energy of the ith atom embedded in the background electron cloud with density ρ_i. The expression of ρ_i is shown in Equation (2).

$$\rho_i = \sum_{j \neq i} \rho_i(r_{ij}) \tag{2}$$

The Morse potential function can accurately express the force and energy between Fe-N, Ni-N, Fe-B and Ni-B atoms, as shown in Equation (3).

$$E_{tot} = \sum D_0 \left[e^{-2\alpha(r-r_0)} - e^{-\alpha(r-r_0)} \right] \tag{3}$$

In Equation (3), there are mainly three parameters, namely, D_0, α, r_0, which represent the binding energy, elastic modulus and atomic spacing of equilibrium position, respectively. According to existing data and debugging, three parameter values can be set as 0.087, 5.14 and 2.05, respectively (Li *et al.*, 2014).

2.2 Establishment of polycrystalline Fe-Ni alloy model

In this paper, Voronoi algorithm is used to generate the polycrystalline workpiece model. The process of Voronoi algorithm is: firstly, the number of grains in the workpiece model is set as N and N coordinate points are randomly generated to serve as the center of these grains, namely the nucleus. Secondly, generate one grain. Choose one point that was randomly generated in the previous step, this point is connected to the other points around it and is bisected vertically. The area enclosed by the vertical bisector is a grain, which is then filled with atoms in a random orientation and an ideal lattice of points. Lastly, repeating the previous two steps to generate all grains in the model. To avoid an unreasonable situation, it

is necessary to remove atoms with smaller distances at the boundary. After completion, the polycrystalline workpiece model can be generated.

In a polycrystalline workpiece model, the number of grains is determined by the size of the workpiece model and the grain. In this paper, the grain size in the Fe-Ni alloy workpiece model will be set to $10 \times 10 \times 10\ nm^3$. Voronoi algorithm was used to generate polycrystalline Fe-Ni alloy workpiece model, and it was found that the number of grain is set to $6 \times 3 \times 2$ (6 grains in X direction, 3 grains in Y direction and 2 grains in Z direction) was the best, because the atomic conversion rate (the number of atoms in the polycrystalline/the number of atoms in the original single crystal) will high up to 99.99%. Therefore, $6 \times 3 \times 2$ grains are filled in single crystal model of size $60 \times 30 \times 20\ nm^3$. In order to save computer memory, the polycrystalline model generated on the basis of the single crystal model will be taken out of size $30 \times 15 \times 10\ nm^3$ part as the research object of this paper.

Figure 1 shows polycrystalline Fe-Ni alloy workpiece model. In the figure, G1–G15 represents different grains, which are distinguished by different colors. The space between the grains is represented as the grain boundary, as shown in purple. The blue area represents CBN grit, red area represents Fe element in Fe-Ni alloy workpiece model and green area represents Ni element. All the atoms in the workpiece are divided into three types: boundary atoms, thermostatic atoms and Newtonian atoms. The boundary atoms remain stationary, the lattice deformation is ignored and the atom is not involved in calculation. The thermostatic atoms are designed to keep the energy of the whole system stable, so their motion needs to be calibrated to keep the temperature constant. The rest are Newtonian atoms, which conform to Newton's classical laws of motion. Both Newtonian and thermostatic atoms are involved in atomic calculation. The boundary atoms and thermostatic atoms thickness are set to 1 nm, and the diameter of CBN grit is set to 10 nm. The CBN grit will move in the negative direction of the X axis (from right to left) according to the designed depth of cut and grinding speed during the simulation. The periodic boundary is used in X-axis and Z-axis to approximate a large (infinite) system by the existing model, which can get an accurate result under the limited computational ability.

2.3 Model parameters in molecular dynamics simulation

In this study, there are 15 groups of MD simulation, and the grinding speed v_s is 12.58, 25.17, 37.75, 50.33 and 62.92 m/s, respectively. The cutting depth of single CBN grit, equivalent to the maximum undeformed chip thickness (a_{gmax}) is 0.9, 1.8 and 2.7 nm, respectively, as shown in Table 1. During the whole simulation process, the grinding distance is 20 nm and the step length is 1 fs (Stadler *et al.*, 1997). The initial temperature of the workpiece is 293 K which is set by using a random number generator with the specified seed to scale the velocity of the atoms.

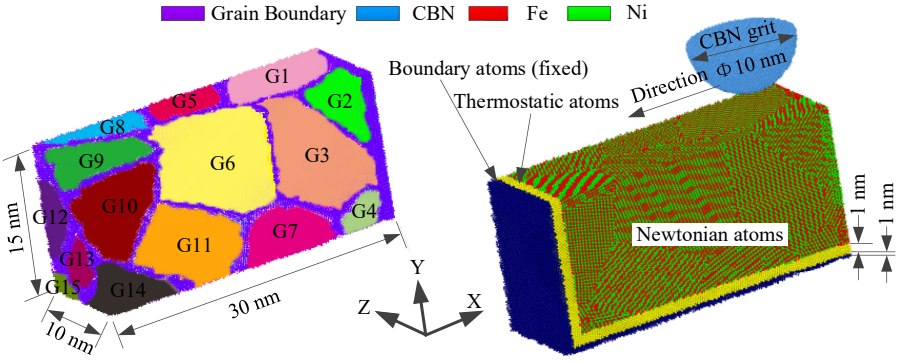

Figure 1.
Fe-Ni alloy workpiece model in MD simulation

During the whole grinding process, there is a considerable amount of energy transmitted to the thermostat atoms, and heat dissipation is carried out in the process of the MD simulation to keep the thermostatic atoms at the constant temperature of 293 K, by adjusting the atom velocities at every five computational time steps using the velocity rescaling method.

All MD simulations are completed using the classical MD package large-scale atomic/molecular massively parallel simulator (LAMMPS). All atomic information will output a dump file at regular intervals as required by the settings. Force, stress, temperature and other information during the grinding simulation will be written in the log file and output. After the simulation, the excel software was used to deal with the force, stress and temperature, and the visualization software OVITO (Stukowski, 2009) was used to open the dump file. The crystal structure and dislocation evolution were analyzed through common neighbor analysis (CNA) and dislocation extraction algorithm (DXA) (Stukowski *et al.*, 2012).

3. Experimental setup

Although the MD simulation and practical grinding experiment differ greatly in the scales of workpiece size and process parameters, the experimental results can verify to some extent whether the simulation process is reasonable and explain the mechanisms of material removal and ground surface generation from the perspective of material microstructure. Therefore, grinding experiments are conducted in this study for the grinding of FeNi alloy under conventional process parameters. The machined specimens are polished and etched, and the thickness of the SSD layer is examined by electron scanning microscope. The measured results are compared with the simulation results for analysis, so as to qualitatively study the effects of grinding parameters on crystal structures, dislocations and SSD.

The grinding experiment is conducted on the Carver S600A machining center. The CBN grinding wheel has a diameter of 100 mm and a width of 6 mm with resin bond. The grinding parameters in the experiment are given as follow: grinding speed v_s = 25.17, 37.75 and 50.33 m/s, work speed v_w = 10 mm/s, depth of cut a_p = 2, 6 and 10 μm. The workpiece material is maraging steel, as mentioned in Section 2.1. The experimental setup is shown in Figure 2.

To facilitate the detection of SSD layer of the ground surface, each workpiece is cut into a size of 12 × 15 × 2 mm after grinding. After the experiment, each specimen is pretreated at first by mechanical polishing using a polishing machine as well as hand polishing by sandpaper. Once the polishing is done, the formula of corrosion solution for the maraging steel needs to be deployed. Through the literature review and experiment investigation, it is found that 10% nitric acid alcohol (100 ml ethanol + 10 ml nitric acid) is able to corrode the surface of the specimen well, so that better observation result of specimen can be achieved. Then the specimen should be cleaned using an ultrasonic cleaner with alcohol or acetone, in order to further improve the detection effectiveness. When all the above pretreatment steps are completed, the specimens will be examined by an electron scanning microscope (SEM), QUANTA 250 to detection subsurface status.

Table 1. Computational parameters used in MD simulation

Properties	Fe-Ni alloy workpiece	CBN tool
Dimension	30 × 15 × 10 (nm^3)	R5 (nm)
Number of atoms	400,938	44,408
Time step (fs)	1	
Initial temperature (K)	293	
Grinding velocity (m/s)	12.58, 25.17, 37.75, 50.33, 62.92	
Cutting depth (nm)	0.9, 1.8, 2.7	
Grinding distance (nm)	20	

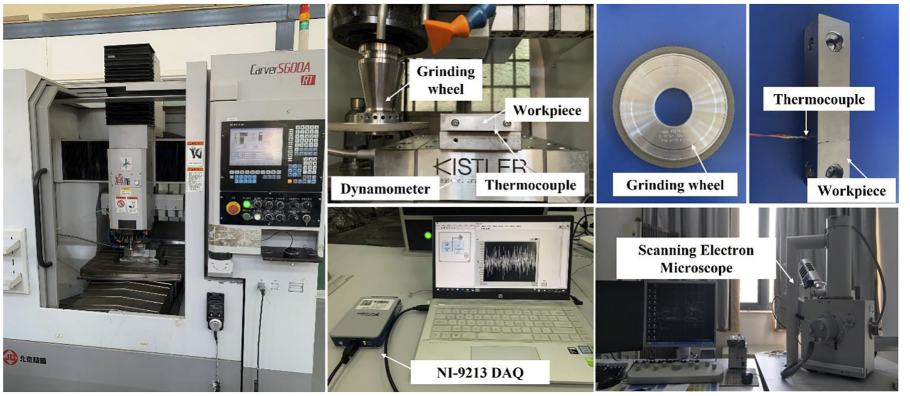

Figure 2.
Schematic diagram of experimental setup

4. Results and discussions

4.1 Transformation of crystal structures

As shown in Figure 3, a cross section diagram of the workpiece at Z = 5 nm under the grinding speed of 37.749 m/s and the depth of cut of 1.8 nm is plotted. In Figure 3a, the CBN grit does not contact the workpiece at the initial time of the simulation. When the grit contacts the workpiece with the setting cutting depth, it will move in the negative direction along the X-axis. The cross section and grain boundaries (shown in the black dotted line) can be clearly found in Figure 3a, and the grain orientation can be obviously identified at the same time.

When the CBN grit continues moving to $l = 5$ nm, as shown in Figure 3b, it is found that the arrangement of atoms in the position of the grit is disordered. In addition, the atoms in front of the CBN grit travel in a straight line with the grit. However, due to the protection of the grain boundaries, the arrangement of atoms within a grain that does not contact the grit will not be disordered (as expressed in white dotted lines).

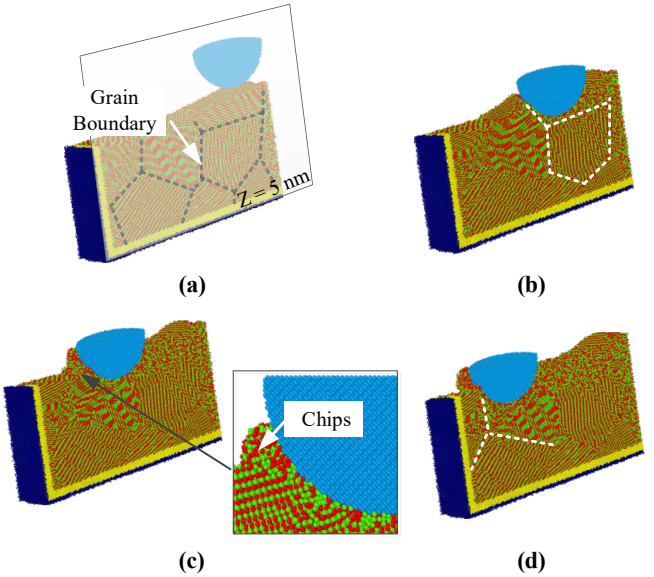

Figure 3.
Grinding process at (a) 0, (b) 5, (c) 10, and (d) 15 nm grinding distance in MD simulation (v_s = 37.75 m/s, a_{gmax} = 1.8 nm)

When the grit keeps moving to l = 10 nm, as shown in Figure 3c, more and more atoms in front of the CBN grit are accumulated, and thus these atoms are forming the chips. Some chips will follow the moving direction of the grit and form larger chips, while the other will flow to both sides of the grit and form a groove. When the grit moves to l = 15 nm, as shown in Figure 3d, the grain boundaries produce larger deformation (white dotted lines), because in the presence of large amounts of dislocations, the gaps can store larger deformation energy.

Figure 4 demonstrates the crystal structure with a cross section diagram of the workpiece at Z = 5 nm when the grinding speed is 12.58 m/s and the cutting depth is 1.8 nm. In Figure 4a, the CBN grit does not contact the workpiece when grinding distance is 0 nm and the atomic structure at the grain boundaries is amorphous because of the complex arrangement of atoms at the grain boundaries and the presence of a large number of dislocations.

As shown in Figure 4b, the number of amorphous structures increases when the grit moves to 10 nm, which is due to the obvious deformation inside the grain and at the grain boundaries under the grinding force as well as the grinding temperature, which makes the atoms rearrange. Most of the atoms that undergo the rearrangement will form irregular amorphous structures, and only a small portion will form regularly arranged atomic crystal structures, as shown in the areas A-A and B-B, which are mainly FCC crystal structures and dense-array hexagonal crystal structures (HCP).

When the grit continues to move to 20 nm in Figure 4c, more of the BCC structures transform into amorphous structure, which is due to the increase of grinding temperature with the larger grinding distance. In addition, the surface of the workpiece is also considered as an amorphous structure, because no atoms is found directly paired with it on the surface of the workpiece, they will exist as individual atoms, so this part of the atomic structure will be considered as an amorphous structure.

The variations of BCC structure, amorphous structure and other structures with different grinding speeds and cutting depths are illustrated in Figure 5. With increasing grinding speed, the reduction of BCC structures appears upward trend (Figure 5a). The higher the grinding speed results in the higher the energy, and thus, more impact of the grit on the workpiece. Therefore, the more the BCC structures will be destroyed and the reduction in the number of BCC structures will increase.

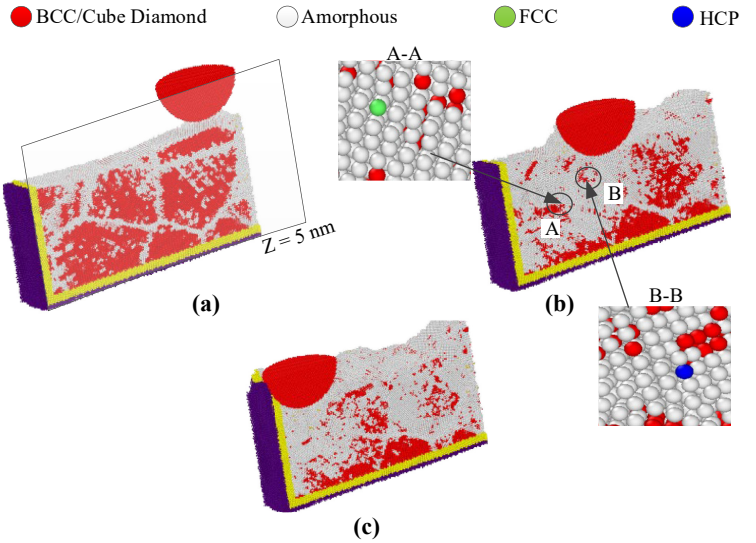

Figure 4.
Crystal structure in grinding process at (a) 0, (b) 10, and (c) 20 nm grinding distance in MD simulation (v_s = 12.58 m/s, a_{gmax} = 1.8 nm)

On the contrary, the variation of amorphous and other (FCC and HCP) structures shows an opposite trend compared with that of BCC structures, as shown in Figure 5b and c. Amorphous structures increment presents upward trend. The destruction of the BCC structures will result in an increase of a large number of amorphous structures and a small number of other regularly arranged crystal structures, such as FCC and HCP.

At the same grinding speed, greater cutting depth results in the more atoms being removed by the grit, and more crystal structures will be destroyed. Similarly, most of the destroyed BCC crystal structures are transformed into amorphous, FCC and HCP structures, so the quantities of these structures will increase with the larger cutting depth.

4.2 Evolution of dislocations

Dislocations have an important influence on the mechanical properties of the materials, mainly in terms of toughness and strength. The more dislocations are produced during the machining process, the higher the strength and the worse the toughness will be achieved by the workpiece. The MD images that show the dislocation evolution of Fe-Ni alloy with different grinding distances when the grinding speed is 12.58 m/s and the depth of cut is 0.9 nm are demonstrated in Figure 6. All images and data are obtained from OVITO, by using DXA module.

After energy minimization, dislocations are mainly concentrated in three regions, namely the grain boundaries of G6-G7-G11, G6-G11 and G11-G14, as shown in Figure 6a at A-A, B-B

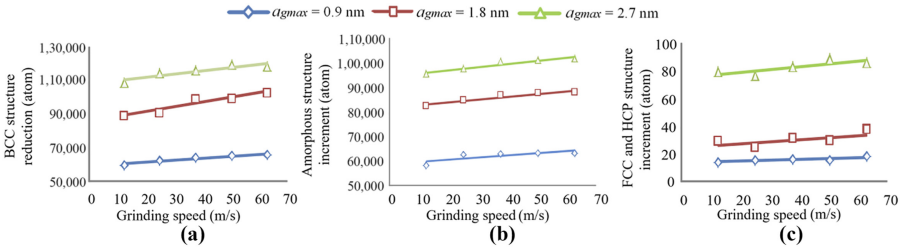

Figure 5.
Variations of crystal structures with different grinding speeds and cutting depths. (a) BCC, (b) Amorphous, and (c) FCC and HCP

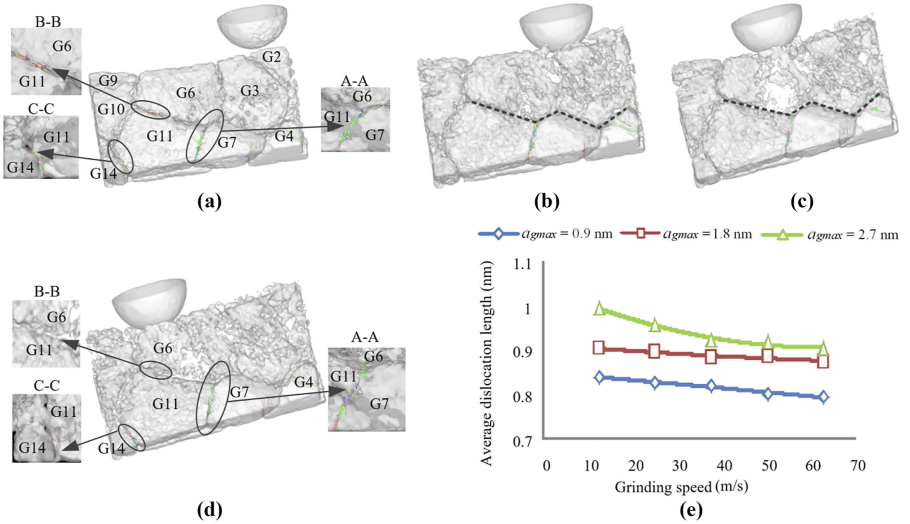

Figure 6.
Dislocation evolution in grinding process at (a) 0, (b) 5, (c) 10 and (d) 15 nm grinding distance in MD simulation (v_s = 12.58 m/s, a_{gmax} = 0.9 nm), and (e) evolution of the average dislocation length with various grinding speeds and cutting depths

and C-C. The dislocations at the grain boundaries are caused by their own polycrystalline structure and the rearrangement of atoms during energy minimization.

As shown in Figure 6b and c, some of the dislocations at the grain boundaries have been gradually reduced when the grit moves to 5 nm and 10 nm, which are caused by the deformation of the grain boundaries under the grinding force and the grinding temperature as well as the heat treatment. In addition, it can be clearly seen from Figure 6b, grain below grain boundaries (black dotted line) is not affected. This further proves that grain boundaries have the function of protecting grain the above mentioned.

When the abrasive grains move to 15 nm, a comparison of A-A, B-B and C-C in Figure 6a and d shows that the dislocations at A-A and C-C are significantly reduced, while those at B-B disappear completely. Furthermore, all dislocations occur at grain boundaries, while no dislocations occur inside the grains, which indicate that grain boundaries are more fragile and more prone to deformation than grains.

The evolution of average dislocation length with various grinding speeds and cutting depths is plotted in Figure 6e. The average dislocation length describes the dislocation at any location in the material, and is a combination of the overall dislocation length of the workpiece and the model volume, which can reflect the dislocation more accurately.

At the same cutting depth, the average dislocation length decreases with the increase of grinding speed. The excessive speed shortens the atomic rearrangement time for dislocation generation, which reduces the average dislocation. As a result, the atoms will move more easily and the material will be more prone to deformation, so the strength of the workpiece will be reduced while the toughness will be improved.

When the grinding speed remains the same the average dislocation length increases as the cutting depth increases. This is because the grinding force and temperature induced by the larger cutting depth will drive the atoms to move faster and thus produce more dislocations. The dislocations will prevent the atoms from moving with increasing average dislocation length and the workpiece will become less deformable, so the strength of the workpiece will increase while the toughness will decrease.

4.3 Analysis of grinding force and temperature

The conventional grinding force comes from two sources: first is the resistance generated when the workpiece material undergoes elastic-plastic deformation during the grinding process; and second is the friction between the abrasive grits and the workpiece surface. In contrast, the MD simulation reveals that the source of nanoscale grinding force is mainly the interaction force between atoms.

The evolution of grinding force with grinding distance when grinding speed is 12.58 m/s and the cutting depth is 1.8 nm is demonstrated in Figure 7a. It can be observed that the whole grinding process is divided into three phases. In Phase I, the grit penetrates the workpiece

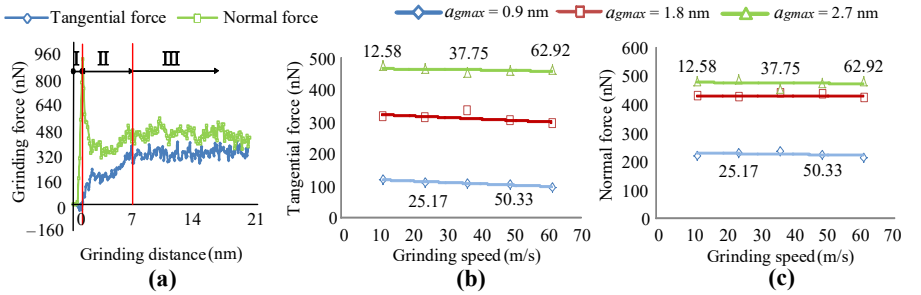

Figure 7.
(a) The changes of grinding force with the grinding distance (v_s = 12.58 m/s, a_{gmax} = 1.8 nm), and the variations of (b) tangential and (c) normal forces with different grinding speeds and cutting depths

until reaching the cutting depth, and the unstable forces are produced in the initial grinding stage (Phase II) when the grit moves around 1 nm. Phase III is the stable grinding phase so that the fluctuations of the forces are little.

Due to the penetration of the grit to the workpiece, a large normal force is generated in Phase I, while the tangential force changes a little. Once the grit starts to move along the workpiece surface, the normal force drops sharply from 820 nN to 360 nN, but still has great fluctuation in Phase II. Both tangential and normal forces are in an unstable status at this stage. In contrast, Phase III is stable grinding phase that forces have little fluctuations, the tangential are normal forces are around 320 nN and 440 nN. The distortion of the atomic lattice when the workpiece atoms are removed and the strain energy is stored. When the removal force is greater than the stored strain energy, the atoms will be removed. At this time, the stored strain energy will disappear suddenly, and the grinding force will decrease suddenly. Therefore, the grinding force will rotate back and forth, resulting in the fluctuation in Phase III.

The variations of tangential and normal force with different grinding speeds and cutting depths are shown in Figure 7b and c. At the same cutting depth, both tangential and normal forces will slightly decrease with the increase of grinding speed. When grinding speed increases, the amorphous structures present increase trend. As the number of amorphous structures increase and the number of BCC structures decrease, the gap in the material will increase, and thus, the grinding force will decrease. When the grinding speed remains the same, both tangential force and normal force increase with the increase of depth of cut. The greater the depth of cut, the more atoms the grit will contact, and the more interatomic forces the grit needs to resist, therefore, the grinding forces show slight increasing trend.

To qualitatively, analyze the trends of grinding forces and temperature in MD simulation, the macrogrinding experiments are performed with the parameters in Table 2. The maximum undeformed chip thickness a_{gmax} is converted to the theoretical depth of cut by Equation (4).

$$a_{gmax} = 2\lambda \frac{v_w}{v_s} \sqrt{a_p d_e} \tag{4}$$

where v_w and v_s are the work speed and grinding speed; a_p is the cutting depth of the grinding wheel, and d_e is the equivalent grinding wheel diameter; λ is the spacing between successive abrasive grits and is assumed to be 150 μm according to the grinding wheel used in this study. The theoretical depth of cut $a_{p.t}$ calculated from the a_{gmax} is difficult to be achieved by the machine tool, and thus, the experimental depth of cut $a_{p.e}$ that is close to the theoretical value is chosen in the experiment.

The grinding forces from the simulation and experiment demonstrate the same trend in Figure 8. Although the simulated and experimental values do not exactly match, they both correctly reflect the trend of the grinding force generated during the grinding process of the Fe-Ni alloy from the microscopic and macroscopic points of view.

Table 2. Grinding parameters in the experiment

No.	Grinding speed v_s (m/s)	Maximum undeformed chip thickness a_{gmax} (nm)	Theoretical depth of cut $a_{p.t}$ (μm)	Experimental depth of cut $a_{p.e}$ (μm)
1	25.17	1.8	2.28	2
2	37.75	1.8	5.13	6
3	50.33	1.8	9.12	10
4	37.75	0.9	1.28	2
5	37.75	1.8	5.13	6
6	37.75	2.7	11.54	10

The grinding temperature in the MD simulation of Fe-NI alloy is also investigated. Figure 9 shows the variations of grinding temperatures with changing grinding speed and cutting depth. It is found that the increasing grinding speed will cause the rise of grinding temperature when the cutting depth keeps constant. On the other hand, the greater the cutting depth results in the higher the grinding temperature, which can be explained by the reason that the grit will contact more atoms in workpiece and break more Fe-Ni metal bonds. The more metal bonds are broken, the more energy is generated and will be transformed to the higher grinding temperature.

The comparisons of simulated and experimental grinding temperatures are shown in Figure 10. Unlike the large difference in grinding force values, the difference in temperature between simulation and experiment is not significant.

By comparisons of the temperature trends, it can be observed that the grinding speed and cutting depth have certain effects on the equilibrium of temperature rise. According to Figure 5b, the lower grinding speed leads to the less quantity of amorphous structure be transformed, so that the workpiece will have the less defects and gaps, and less time is taken to reach temperature equilibrium. Therefore, the grinding temperature can reach equilibrium state rapidly at low grinding speed. Correspondingly, smaller cutting depth can also make less amorphous structure be transformed and less defects and gaps will be produced to balance the grinding temperature in a short time.

4.4 Generation of subsurface damage

SSD can have a great impact on the serviceability of machined workpieces, the most significant of which are the fracture strength and fatigue strength of the workpieces.

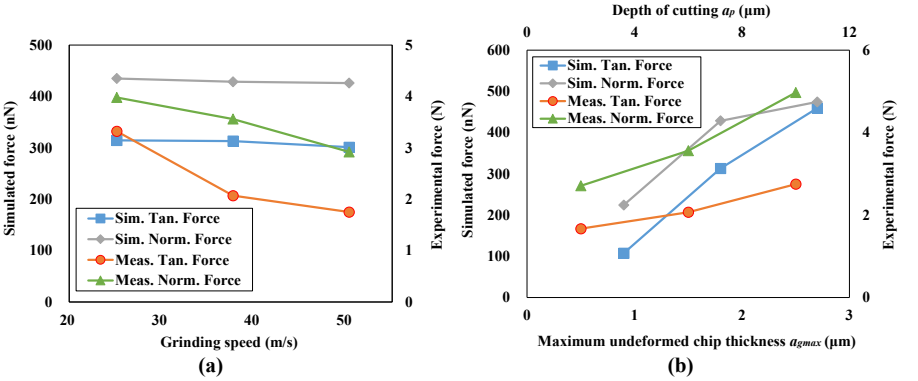

Figure 8.
Comparison of grinding forces with different grinding speeds (a) and cutting depths (b)

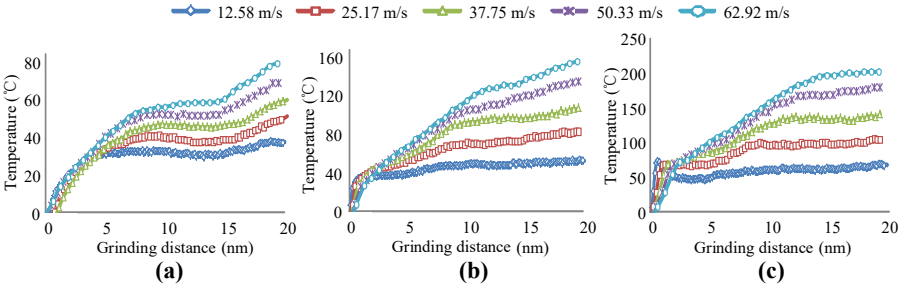

Figure 9.
The changes of grinding temperature with the grinding distance when the cutting depth is (a) 0.9, (b) 1.8 and (c) 2.7 nm

Therefore, it is crucial to study the influence of different grinding process parameters on the SSD layer. As shown in Figure 9, the distance between the newly generated amorphous structure (the newly generated gray area) and the lowermost part of the abrasive grain is the thickness of the SSD layer.

The SSD thickness is positively correlated with the cutting depth because more material removal induces larger force and temperature which cause greater stress and thermal effect zone. In Figure 11a, when the cutting depth increases from 0.9 to 1.8 and 2.7 nm, the SSD thickness enlarges from 5.683 to 7.458 and 8.783 nm, respectively. By horizontal comparison from Figure 9a–e, the SSD thickness decreases by 47.8% with increasing grinding speed when the cutting depth remains at 0.9 nm. This is because the faster the grinding speed, the shorter the contact time between the workpiece surface workpiece and the grit, and therefore the less damage to the subsurface. The reduction about 31.2% and 39.4% of SSD thickness is also discovered when the grinding speed increase from 12.58 to 62.92 m/s at cutting depth of 1.8 and 2.7 nm, respectively.

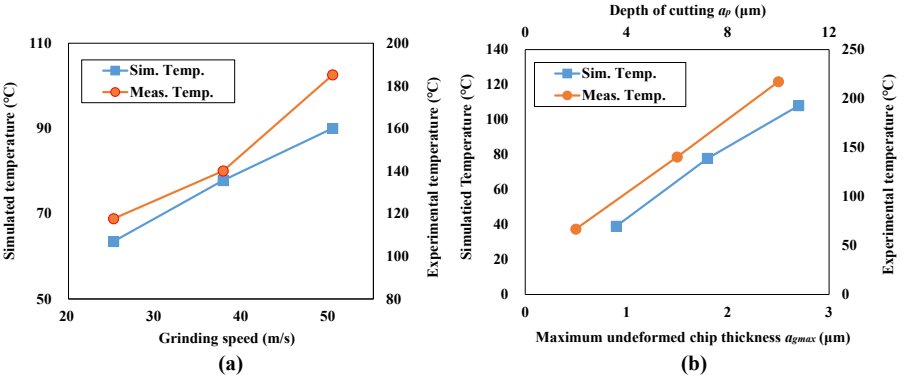

Figure 10.
Comparison of grinding temperature with different grinding speeds (a) and cutting depths (b)

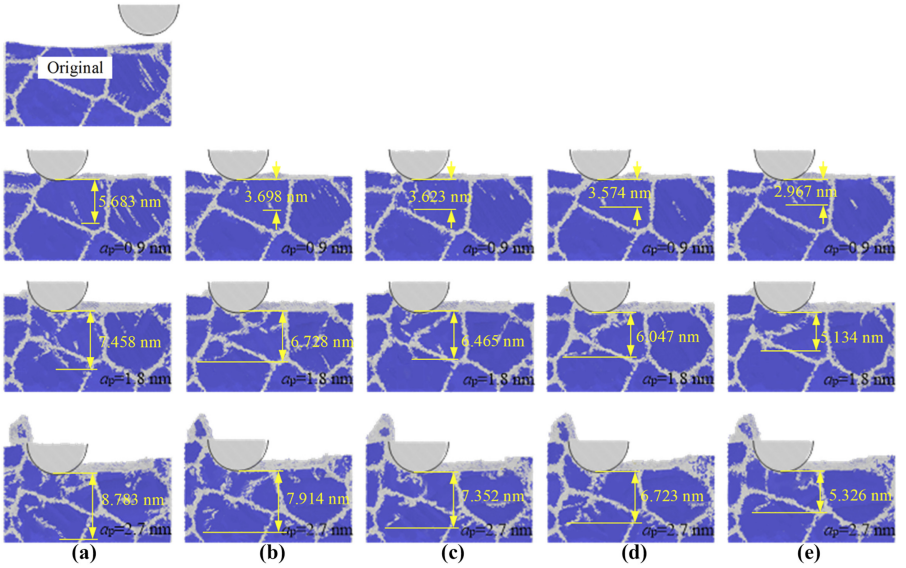

Figure 11.
Subsurface damage thickness at grinding speed of (a) 12.58, (b) 25.17, (c) 37.75, (d) 50.33 and (e) 62.92 m/s in MD simulation

Moreover, it can also be concluded that at lower cutting (0.9 nm), the SSD layer thickness only appears in the grain, while the grain boundaries are not affected, but at higher cutting depth (1.8 nm and 2.7 nm), the SSD layer will connect with the old grain boundaries, resulting in a deeper SSD layer thickness (see Figure 12).

In order to determine the thickness of the SSD layer in the practical grinding process, and then compared with the thickness of the SSD layer in the MD simulation for analysis, the grinding experiments are performed and the SSD layer of ground specimens are detected by the scanning electron microscope. The SEM images of SSD layer with various grinding speeds are shown in Figure 13. By observing each individual image, it can be found that the tissue structures in the damaged layer are affected significantly by the atoms arrangements and transformation from BCC structure to other structures (as shown by the inclined yellow arrows), while the tissue structures of the unaffected part still shows a natural state. The contact time between the grit and workpiece surface are shortened due to the increase of grinding speed, and thus, less atoms are deformed. The thickness of the SSD layer decreased from 3.629 μm to 2.5 μm when the grinding speed changes from 6.28 m/s to 18.84 m/s and the cutting depth keeps constant, which is improved by 31.1%.

With the increase of cutting depth, the thickness of SSD layer shows an increasing trend in Figure 11, which is consistent with the results in the MD simulation as well. The tissue structures in the damaged layer are also inclined with the grinding direction. The higher grinding temperature induced by the increase of cutting depth will damages the crystal structure around the grit, and therefore, the thickness of SSD layer is enlarged. When the grinding speed keeps constant and the cutting depth changes from 2 μm to 10 μm, the thickness of the SSD layer increased sharply from 1.032 μm to 6.484 μm, which deteriorates significantly by around 5 times.

The thickness of the SSD layer is directly related to the grinding speed and cutting depth. Both MD simulation and experimental results reveal that the effect of grinding depth on the

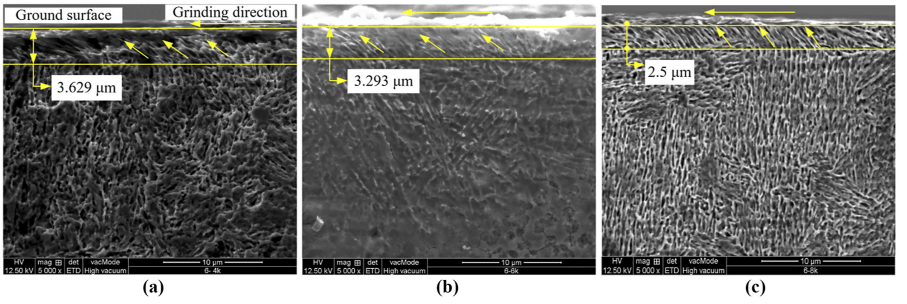

Figure 12.
SEM images of grinding subsurface damage layer thickness at (a) v_s = 25.17 m/s, a_p = 6 μm, (b) v_s = 37.75 m/s, a_p = 6 μm and (c) v_s = 50.33 m/s, a_p = 6 μm

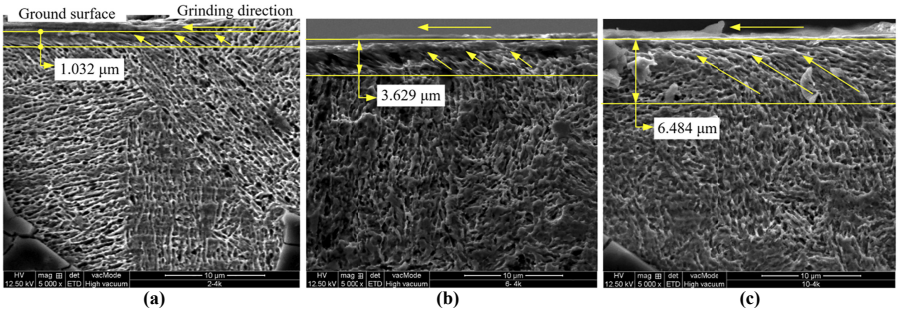

Figure 13.
SEM images of grinding subsurface damage layer thickness at depth of cut of (a) 2, (b) 6 and (c) 10 μm

evolution of SSD layer thickness is greater than that of grinding speed. Compared with macroscopic grinding simulation, which analyzes the damage layer of materials by grinding force, heat and elastic-plastic deformation, MD simulation studies the changes in the internal microstructure of materials from a more microscopic perspective, i.e. atomic removal, crystal structure transformation, dislocation evolution, etc. Although it is difficult to match the numerical results of the MD simulation exactly with the experimental results, it can provide a theoretical basis for the macroscopic grinding process.

5. Conclusion

In this study, the crystal structure, dislocation evolution, grinding force, grinding temperature and SSD in the grinding of Fe-Ni alloy are analyzed by MD simulation and experiments. The conclusions can be drawn as follows:

(1) When CBN grit goes through one of the grains, the arrangement of atoms within the grain will be disordered, but other grains will not be easily deformed due to the protection of the grain boundaries. This is because there are a lot of dislocations and gaps in the grain boundaries and the grain boundaries can store great deformation energy.

(2) Higher grinding speed and larger cutting depth can cause greater impact of grit on the atoms, and more BCC structures will be destroyed. Most BCC structures will transform into the amorphous structures and the other will transform to the FCC and HCP structures under the effects of excessive grinding force and temperature.

(3) The dislocations will appear in grain boundaries due to the rearrangement of atoms in grinding. The higher the grinding speed, the smaller the average dislocation length will be produced because the time of atoms to regenerate dislocations is shortened. On the other hand, larger cutting depth can cause greater force and temperature to make atoms move faster, so that the average dislocation length will be enlarged.

(4) The increase of grinding speed results in the more transformation from BCC to amorphous structures. Thus, more gaps are produced among the atoms and then the grinding force decreases. The enlargement of the cutting depth causes the more atoms being contacted by the grit, and the more interatomic energy needs to consume, which results in the rise of grinding temperature.

(5) The thickness of SSD layer is positively correlated with the cutting depth because more material removal produces larger force and temperature, which causes greater stress and thermal effect zone. The shorter contact time between the grit and workpiece surface induced by the increase of grinding speed prevent more deformation of atoms, and therefore, the thickness of SSD layer becomes smaller.

References

Bonny, G., Pasianot, R.C., Castin, N. and Malerba, L. (2009), "Ternary Fe–Cu–Ni many-body potential to model reactor pressure vessel steels: first validation by simulated thermal annealing", *Philosophical Magazine*, Vol. 89 Nos 34-36, pp. 3531-3546.

Chen, X., Chen, L., Chen, H., Song, B., Zhao, Y., Yu, T. and Zhao, J. (2022), "Meso-scale numerical simulation and experimental verification of single grain grinding TiC–Fe composites", *Ceramics International*, Vol. 48 No. 9, pp. 12299-12310.

Daw, M.S., Foiles, S.M. and Baskes, M.I. (1993), "The embedded-atom method: a review of theory and applications", *Materials Science Reports*, Vol. 9 Nos 7-8, pp. 251-310.

Ding, Z., Sun, J., Guo, W., Jiang, X., Wu, C. and Liang, S.Y. (2022), "Thermal analysis of 3J33 grinding under minimum quantity lubrication condition", *International Journal of Precision Engineering and Manufacturing-Green Technology*, Vol. 9 No. 5, pp. 1247-1265.

Foiles, S.M., Baskes, M.I. and Daw, M.S. (1986), "Embedded-atom-method functions for the fcc metals Cu, Ag, Au, Ni, Pd, Pt, and their alloys", *Physical Review B*, Vol. 33 No. 12, p. 7983.

Guo, X., Li, Q., Liu, T., Zhai, C., Kang, R. and Jin, Z. (2016), "Molecular dynamics study on the thickness of damage layer in multiple grinding of monocrystalline silicon", *Materials Science in Semiconductor Processing*, Vol. 51, pp. 15-19.

Guo, X., Zhai, R., Shi, Y., Kang, R., Jin, Z. and Guo, D. (2020), "Study on influence of grinding depth and grain shape on grinding damage of K9 glass by SPH simulation", *The International Journal of Advanced Manufacturing Technology*, Vol. 106 No. 1, pp. 333-343.

Guo, W., Wu, C., Ding, Z. and Zhou, Q. (2021), "Prediction of surface roughness based on a hybrid feature selection method and long short-term memory network in grinding", *The International Journal of Advanced Manufacturing Technology*, Vol. 112 No. 9, pp. 2853-2871.

Huang, Y., Wang, M., Xu, Y. and Zhu, F. (2021), "Investigation of vibration-assisted nano-grinding of gallium nitride via molecular dynamics", *Materials Science in Semiconductor Processing*, Vol. 121, 105372.

Lan, S. and Jiao, F. (2019), "Modeling of heat source in grinding zone and numerical simulation for grinding temperature field", *The International Journal of Advanced Manufacturing Technology*, Vol. 103 No. 5, pp. 3077-3086.

Lerra, F., Liverani, E., Landi, E. and Fortunato, A. (2022), "Real single grain grinding finite element method simulation for case-hardened steel based on equivalent contact area analysis", *Journal of Manufacturing Science and Engineering*, Vol. 144 No. 1, p. 011008.

Li, B., Ding, Z., Xiao, J. and Liang, S.Y. (2016), "Maraging steel 3J33 phase transformation during micro-grinding", *Materials Letters*, Vol. 164, pp. 217-220.

Li, J., Fang, Q., Liu, Y. and Zhang, L. (2014), "A molecular dynamics investigation into the mechanisms of subsurface damage and material removal of monocrystalline copper subjected to nanoscale high speed grinding", *Applied Surface Science*, Vol. 303, pp. 331-343.

Li, J., Fang, Q., Zhang, L. and Liu, Y. (2015), "The effect of rough surface on nanoscale high speed grinding by a molecular dynamics simulation", *Computational Materials Science*, Vol. 98, pp. 252-262.

Li, P., Guo, X., Yuan, S., Li, M., Kang, R. and Guo, D. (2021), "Effects of grinding speeds on the subsurface damage of single crystal silicon based on molecular dynamics simulations", *Applied Surface Science*, Vol. 554, 149668.

Li, C., Piao, Y., Meng, B., Hu, Y., Li, L. and Zhang, F. (2022), "Phase transition and plastic deformation mechanisms induced by self-rotating grinding of GaN single crystals", *International Journal of Machine Tools and Manufacture*, Vol. 172, 103827.

Liu, Y., Ji, Y., Dong, L., Xie, H., Song, J. and Li, J. (2022), "Effect of grinding depths on SiC nanogrinding behavior based on molecular dynamics", *Applied Physics A*, Vol. 128 No. 1, pp. 1-10.

Lv, Y., Peng, Z., Qu, C. and Zhu, D. (2020), "An adaptive trajectory planning algorithm for robotic belt grinding of blade leading and trailing edges based on material removal profile model", *Robotics and Computer-Integrated Manufacturing*, Vol. 66, 101987.

Pei, Q.X., Lu, C. and Lee, H.P. (2007), "Large scale molecular dynamics study of nanometric machining of copper", *Computational Materials Science*, Vol. 41 No. 2, pp. 177-185.

Peng, R., Tong, J., Tang, X., Huang, X. and Liu, K. (2021), "Application of a pressurized internal cooling method in grinding inconel 718: modeling-simulation and testing-validation", *International Journal of Mechanical Sciences*, Vol. 189, 105985.

Ren, J., Hao, M., Lv, M., Wang, S. and Zhu, B. (2018), "Molecular dynamics research on ultra-high-speed grinding mechanism of monocrystalline nickel", *Applied Surface Science*, Vol. 455, pp. 629-634.

Stadler, J., Mikulla, R. and Trebin, H.R. (1997), "IMD: a software package for molecular dynamics studies on parallel computers", *International Journal of Modern Physics C*, Vol. 8 No. 05, pp. 1131-1140.

Stukowski, A. (2009), "Visualization and analysis of atomistic simulation data with OVITO–the Open Visualization Tool", *Modelling and Simulation in Materials Science and Engineering*, Vol. 18 No. 1, 015012.

Stukowski, A., Bulatov, V.V. and Arsenlis, A. (2012), "Automated identification and indexing of dislocations in crystal interfaces", *Modelling and Simulation in Materials Science and Engineering*, Vol. 20 No. 8, 085007.

Sun, Y., Jin, L., Gong, Y., Wen, X., Yin, G., Wen, Q. and Tang, B. (2022), "Experimental evaluation of surface generation and force time-varying characteristics of curvilinear grooved micro end mills fabricated by EDM", *Journal of Manufacturing Processes*, Vol. 73, pp. 799-814.

Wan, L., Liu, Z., Deng, Z., Li, L. and Liu, W. (2018), "Simulation and experimental research on subsurface damage of silicon nitride grinding", *Ceramics International*, Vol. 44 No. 7, pp. 8290-8296.

Wang, Q., Fang, Q., Li, J., Tian, Y. and Liu, Y. (2019), "Subsurface damage and material removal of Al–Si bilayers under high-speed grinding using molecular dynamics (MD) simulation", *Applied Physics A*, Vol. 125 No. 8, pp. 1-9.

Xu, Y., Wang, M., Zhu, F., Liu, X., Chen, Q., Hu, J., . . . and Liu, Y. (2019), "A molecular dynamic study of nano-grinding of a monocrystalline copper-silicon substrate", *Applied Surface Science*, Vol. 493, pp. 933-947.

Yeqiong, W.U. and Mufu, Y.A.N. (2011), "Effects of lanthanum and cerium on low temperature plasma nitrocarburizing of nanocrystallized 3J33 steel", *Journal of Rare Earths*, Vol. 29 No. 4, pp. 383-387.

Zhang, J., Sun, T., Yan, Y. and Liang, Y. (2009), "Molecular dynamics study of scratching velocity dependency in AFM-based nanometric scratching process", *Materials Science and Engineering: A*, Vol. 505 Nos 1-2, pp. 65-69.

Zhang, Y., Wang, Q., Li, C., Piao, Y., Hou, N. and Hu, K. (2022), "Characterization of surface and subsurface defects induced by abrasive machining of optical crystals using grazing incidence X-ray diffraction and molecular dynamics", *Journal of Advanced Research*, Vol. 36, pp. 51-61.

Zhao, P., Zhao, B., Pan, J. and Wu, J. (2022), "Nano-grinding process of single-crystal silicon using molecular dynamics simulation: nano-grinding parameters effect", *Materials Science in Semiconductor Processing*, Vol. 143, 106531.

Zhou, J., He, Y., Shen, J., Essa, F.A. and Yu, J. (2021), "Ni/Ni3Al interface-dominated nanoindentation deformation and pop-in events", *Nanotechnology*, Vol. 33 No. 10, 105703.

Zhou, K., Liu, J., Xiao, G., Huang, Y., Song, K., Xu, J. and Chen, B. (2021), "Probing residual stress evolution of titanium alloy due to belt grinding based on molecular dynamics method", *Journal of Manufacturing Processes*, Vol. 66, pp. 446-459.

Corresponding author
Chongjun Wu can be contacted at: wcjunm@dhu.edu.cn